

See discussions, stats, and author profiles for this publication at: <https://www.researchgate.net/publication/49696176>

Thermodynamics of the Formaldehyde–Water and Formaldehyde–Ice Systems for Atmospheric Applications

ARTICLE *in* THE JOURNAL OF PHYSICAL CHEMISTRY A · JANUARY 2011

Impact Factor: 2.69 · DOI: 10.1021/jp108907u · Source: PubMed

CITATIONS

21

READS

140

3 AUTHORS:



Manuel Barret

ID² Solutions Innovantes

21 PUBLICATIONS 175 CITATIONS

SEE PROFILE



S. Houdier

University Joseph Fourier - Grenoble 1

40 PUBLICATIONS 666 CITATIONS

SEE PROFILE



Florent Domine

Laval University

154 PUBLICATIONS 3,975 CITATIONS

SEE PROFILE

Thermodynamics of the Formaldehyde–Water and Formaldehyde–Ice Systems for Atmospheric Applications

Manuel Barret, Stephan Houdier, and Florent Domine*

CNRS, Laboratoire de Glaciologie et Géophysique de l'Environnement, BP 96, 54 Rue Molière, 38402 Saint Martin d'Hères Cédex, France

Received: September 17, 2010; Revised Manuscript Received: November 24, 2010

Formaldehyde (HCHO) is a species involved in numerous key atmospheric chemistry processes that can significantly impact the oxidative capacity of the atmosphere. Since gaseous HCHO is soluble in water, the water droplets of clouds and the ice crystals of snow exchange HCHO with the gas phase and the partitioning of HCHO between the air, water, and ice phases must be known to understand its chemistry. This study proposes thermodynamic formulations for the partitioning of HCHO between the gas phase and the ice and liquid water phases. A reanalysis of existing data on the vapor–liquid equilibrium has shown the inadequacy of the Henry's law formulation, and we instead propose the following equation to predict the mole fraction of HCHO in liquid water at equilibrium, $X_{\text{HCHO,liq}}$, as a function of the partial pressure P_{HCHO} (Pa) and temperature T (K): $X_{\text{HCHO,liq}} = 1.700 \times 10^{-15} e^{(8014/T)} (P_{\text{HCHO}})^{1.105}$. Given the paucity of data on the gas–ice equilibrium, the solubility of HCHO and the diffusion coefficient (D_{HCHO}) in ice were measured by exposing large single ice crystals to low P_{HCHO} . Our recommended value for D_{HCHO} over the temperature range 243–266 K is $D_{\text{HCHO}} = 6 \times 10^{-12} \text{ cm}^2 \text{ s}^{-1}$. The solubility of HCHO in ice follows the relationship $X_{\text{HCHO,ice}} = 9.898 \times 10^{-13} e^{(4072/T)} (P_{\text{HCHO}})^{0.803}$. Extrapolation of these data yields the P_{HCHO} versus $1/T$ phase diagram for the H_2O –HCHO system. The comparison of our results to existing data on the partitioning of HCHO between the snow and the atmosphere in the high arctic highlights the interplay between thermodynamic equilibrium and kinetics processes in natural systems.

Introduction

Formaldehyde (HCHO) is an intermediate in the atmospheric oxidation of methane and it is also emitted directly by anthropogenic and natural sources.^{1–3} HCHO is the most abundant carbonyl compound in the atmosphere and is involved in numerous key atmospheric chemistry processes. The major HCHO sink in the atmosphere is its photolysis, which produces HO_x radicals,^{4–6} therefore impacting the oxidative capacity of the atmosphere. Since it is soluble in water, HCHO may be scavenged from the gas phase by rain or fog droplets.^{7–11} This scavenging has a strong impact on clouds chemistry, for instance, the oxidation of dissolved HCHO in cloudwater droplets by OH radicals is the most important sink for the OH radical in clouds.¹² HCHO is also likely to be efficiently scavenged by ice crystals in the atmosphere or taken up by snow crystals on the ground, because HCHO forms a solid solution with ice.^{13,14} HCHO can be emitted by the snowpack both from photochemical sources and by the degassing of snow grains supersaturated in HCHO.¹⁵ The Arctic snowpack has thus been shown to be a major reservoir of HCHO and its emission to the atmosphere may strongly impact the chemistry of the polar atmospheric boundary layer.^{16–18} The partitioning of HCHO between the gas phase and water or ice is thus a crucial parameter to understand atmospheric chemistry and in particular to develop multiphase chemistry models.

Several studies have been performed to determine the vapor–liquid equilibrium of HCHO.^{19–25} Results are often reported in terms of the Henry's law coefficient H defined as $H = [\text{HCHO}]/P_{\text{HCHO}}$, where $[\text{HCHO}]$ is the concentration in mol

L^{-1} (M) of HCHO in the water solution and P_{HCHO} the partial pressure in the gas phase. The different relevant studies show large discrepancies in the H values obtained, which seem to depend on the HCHO concentration in the liquid phase. For instance, H_{HCHO} values are in the range 1840–6440 M atm^{-1} at 295 K²⁵ and between 3000 and 5200 M atm^{-1} at 293 K.²⁰

Only a small amount of data are available on the partitioning of formaldehyde between air and ice. Burkhart et al.²⁶ calculated partitioning coefficients by exposing laboratory-made “snow” obtained by freezing water in liquid nitrogen to a formaldehyde flux for experiments of a maximum duration of 44 h. They calculated the ice–air partition coefficient (K_D), which is defined as the ratio of the HCHO concentration in snow $[\text{HCHO}]_{\text{snow}}$ over the HCHO partial pressure P_{HCHO} : $K_D = [\text{HCHO}]_{\text{snow}}/P_{\text{HCHO}}$. However this partition coefficient K_D may not be the actual equilibrium parameter since the concentration observed in ice results from several processes including adsorption at the surface of snow, diffusion and solubility in the bulk of ice and in small angle boundaries. Because diffusion in ice is orders of magnitude lower than in liquid solutions, equilibrium in the bulk of ice may not have been reached in such short experiments. Perrier et al.¹⁴ obtained diffusion profiles of HCHO in ice single crystals from which they calculated its solubility and diffusion coefficient in ice. Only two experiments were performed, which was not sufficient to determine the thermodynamic parameters governing the temperature and partial pressure dependence of the solubility. However, the value of the diffusion coefficient that they obtained at -15°C , $D_{\text{HCHO}}(-15^\circ\text{C}) = 8 \times 10^{-11} \text{ cm}^2 \text{ s}^{-1}$, indicates that the snow used by Burkhart et al.²⁶ probably was not at thermodynamic equilibrium. Their partition coefficients may thus have been underestimated.

* To whom correspondence should be addressed. Phone (+33) 476 82 42 69. E-mail: florent@lgge.obs.ujf-grenoble.fr.

The aim of this study is to propose thermodynamic formulations that will allow the quantification of the solubility of HCHO in both water and ice for conditions relevant to the atmosphere. For the HCHO–water system, a literature review was performed to propose an original formulation that we believe is more appropriate than the Henry's Law formulation to describe equilibria in this system. For the HCHO–ice system, the lack of existing data renders extra measurements mandatory. In a manner similar to Perrier et al.,¹⁴ we exposed large ice single crystals to known P_{HCHO} values. After several weeks of exposure, serial sectioning of the doped crystals yielded the diffusion coefficient and the solubility of HCHO in ice as a function of T and P_{HCHO} .

Our study of the solid solutions of HCHO in ice was used to propose a formulation of the ice–HCHO equilibrium and to construct the solidus of the phase diagram of the H_2O –HCHO system. This complements the temperature–composition phase diagram previously proposed by Soboleva et al.²⁷ The combination of existing vapor pressure equilibria for the HCHO–water system and of our new vapor pressure data on the HCHO–ice system also allowed to build the pressure–inverse temperature phase diagram and to calculate the ice–water partition coefficient of HCHO.

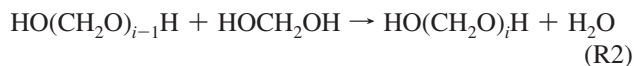
Thermodynamics of Liquid Solutions

In what follows, we will express HCHO concentrations in molar fraction X_{HCHO} , which is the appropriate quantity for thermodynamic considerations. The HCHO concentration $[\text{HCHO}]$ in mol L^{-1} can be calculated from X_{HCHO} according to the following relationship

$$[\text{HCHO}] = \frac{\rho X_{\text{HCHO}}}{X_{\text{HCHO}} M_{\text{HCHO}} + (1 - X_{\text{HCHO}}) M_{\text{H}_2\text{O}}} \quad (1)$$

where ρ is the density of the solution expressed in g L^{-1} , and M_{HCHO} and $M_{\text{H}_2\text{O}}$ are the molar masses of HCHO and H_2O in g mol^{-1} . For the dilute liquid solutions of atmospheric interest, ρ is close to the density of pure water and a value of 1000 g L^{-1} may be used.

Previous Studies. Formaldehyde and water react to yield methylene glycol and subsequently polyoxomethylene glycols following reactions R1 and R2



The equilibrium constant for hydration of formaldehyde (R1) being close to 2×10^3 at atmospheric temperatures,²⁸ free HCHO can be neglected and methylene glycols largely predominate. When describing the vapor–liquid equilibrium, the Henry's law coefficient that is experimentally measured is the effective Henry's law coefficient, H^* , which is the ratio between the overall concentration of formaldehyde in all its forms (i.e., polyoxomethylene glycols and free HCHO) and the HCHO partial pressure. Given reactions R1 and R2, it is not surprising that significant deviation from a constant Henry's law coefficient is observed at high formaldehyde concentrations.

The data of Betterton and Hoffmann²¹ are commonly used as reference values with $H^*(298 \text{ K}) = 2.97 \times 10^3 \text{ M atm}^{-1}$ obtained for $X_{\text{HCHO}} = 2.0 \times 10^{-5}$. We can extrapolate this value

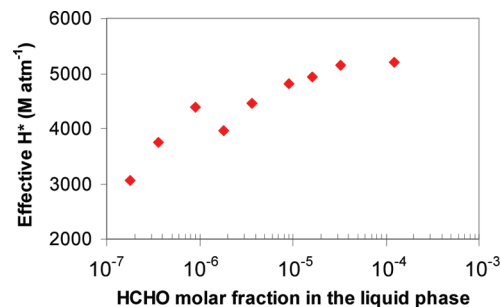


Figure 1. Effective Henry's law coefficient calculated from the data of Dong and Dasgupta²⁰ obtained at 293 K. Solubility increases with the HCHO liquid molar fraction.

to 293 K by using the partial molar enthalpy of vaporization $\Delta h_{\text{vap}} = 60.3 \text{ kJ mol}^{-1}$ calculated subsequently in this study, and we obtain $H^*_{\text{Betterton}}(293 \text{ K}) = 5.2 \times 10^3 \text{ M atm}^{-1}$. At higher concentrations, we can calculate H^* from the data of Blair and Ledbury,¹⁹ who performed experiments for molar fractions between 5.6×10^{-2} and 0.3. Values of $H^*_{\text{Blair}}(293 \text{ K})$ are in the range $7\text{--}10 \times 10^3 \text{ M atm}^{-1}$ with the highest values obtained for the highest concentrations. In an early study by Dong and Dasgupta,²⁰ a concentration dependence of H^* values was observed for X_{HCHO} as low as $X_{\text{HCHO}} = 2 \times 10^{-7}$ (Figure 1). This concentration dependence was not expected at low concentrations where aqueous solutions are more likely to behave as ideal solutions. This trend in the increase of H^* with increasing aqueous concentration is also confirmed by the recent study of Oancea et al.²⁵ At 295 K they obtained H^* values ranging from 3×10^3 to $6 \times 10^3 \text{ M atm}^{-1}$ for HCHO aqueous molar fractions ranging from 10^{-5} to 10^{-3} .

Dong and Dasgupta²⁰ proposed to use a power law to describe their results (eq 2)

$$\log[P_{\text{HCHO}}(\text{atm})] = 0.9261 \log(X_{\text{HCHO}}) - 2.2942 \quad (2)$$

The authors mentioned that eq 2 has a “striking ability to fit Blair and Ledbury's data¹⁹” who performed experiments at aqueous concentrations several orders of magnitude higher than the concentration range from which eq 2 was derived.

They emphasized that such a relationship was only empirical. However it is possible to derive a similar relationship based on the laws of Gibbs–Duhem and Raoult, by introducing a vapor depression factor n_L that expresses the decrease in volatility of the solvent with the addition of the dissolved species.

Proposed Relationship for the Liquid–Vapor Equilibrium. Thermodynamics of Liquid–Vapor Equilibrium. The vapor pressure of water in such a mixture can be calculated using Raoult's law with reduction of the vapor pressure of the solvent.²⁹ It assumes that the decrease in the solvent vapor pressure is characterized by the vapor depression factor n_L according to

$$P_{\text{H}_2\text{O}}(X_{\text{HCHO}}, T) = (1 - n_L X_{\text{HCHO}}) P^*_{\text{H}_2\text{O}}(T) \quad (3)$$

where $P^*_{\text{H}_2\text{O}}$ (in Pa) is the saturating vapor pressure of water, and X_{HCHO} is the molar fraction of HCHO in the liquid phase including free HCHO and hydrated glycols.

When combining the laws of Raoult and Gibbs–Duhem, we can derive eq 4, which was successfully used to describe the solubility of acidic gases in water or ice solutions^{30–32}

$$P_{\text{HCHO}}(X_{\text{HCHO}}, T) = (X_{\text{HCHO}})^{n_L} A(T) \quad (4)$$

where $A(T)$ is a coefficient whose temperature dependence is related to the partial molar enthalpy of vaporization of HCHO, Δh_{vap} , so that eq 4 can be written (using Clapeyron's law and the hypothesis that n_L and Δh_{vap} are not temperature-dependent)

$$P_{\text{HCHO}}(X_{\text{HCHO}}, T) = (X_{\text{HCHO}})^{n_L} A_0 \exp\left(-\frac{\Delta h_{\text{vap}}}{RT}\right) \quad (5)$$

where A_0 (in Pa) is a constant. Equation 5 is equivalent to Henry's law only if $n_L = 1$.

Experimental studies have shown that the total vapor pressure $P_{\text{tot}} = P_{\text{H}_2\text{O}} + P_{\text{HCHO}}$ of the system decreased with increasing HCHO concentrations. This pressure decrease has been observed by Brandani et al.³³ for temperatures between 313 and 363 K and X_{HCHO} between 2.95×10^{-3} and 0.3. The same trend can be observed at 295 K in the data of Oancea et al.²⁵ Our proposed formulation should be able to explain such variations since we can derive from eqs 3 and 5 the X_{HCHO} dependence on the total vapor pressure P_{tot} (eq 6). As a result we see that for a given temperature, P_{tot} is a linear function of X_{HCHO} whose slope depends on n_L and on the difference between the vapor pressure terms related to HCHO and H_2O

$$\frac{\partial P_{\text{tot}}}{\partial X_{\text{HCHO}}}(X_{\text{HCHO}}, T) = n_L \left[A_0 \exp\left(-\frac{\Delta h_{\text{vap}}}{RT}\right) - P_{\text{H}_2\text{O}}^*(T) \right] \quad (6)$$

In order to determine the values of n_L , A_0 , and Δh_{vap} , we made a synthesis of available experimental studies by using eq 5 rather than Henry's law which appears inadequate to describe the equilibrium between the gas phase and HCHO aqueous solutions.

Reinvestigated Data and Optimization. We used data from different studies^{19–21,23,25} providing 116 experimental points for the $(P_{\text{HCHO}}, X_{\text{HCHO}})$ equilibrium over a large range of experimental conditions, covering the temperature range 278–423 K, the X_{HCHO} range 1.8×10^{-7} to 0.6, and the P_{HCHO} range 3.3×10^{-4} to 4×10^5 Pa.

We first considered studies that reported HCHO equilibrium data at different temperatures^{20,21,23} to derive the partial molar enthalpy of vaporization Δh_{vap} . Values of 59.8, 61.2, and 59.3 kJ mol⁻¹ were obtained from the data of Betterton and Hoffmann, Albert et al., and Oancea et al., respectively, yielding a standard deviation of only 1.4 kJ mol⁻¹ within these data sets. The mean value of $\Delta h_{\text{vap}} = 60.3 \pm 1.4$ kJ mol⁻¹ will be used in what follows.

For each $\{P_{\text{HCHO}}, T\}$ available set of values,^{19–21,23,25} we used a least absolute deviation method to find the optimal set of parameters A_0 and n_L that minimizes the sum of absolute errors (SAE) between the logarithmic values of X_{HCHO} calculated with eq 5 and the experimental data. The best agreement (Figure 2) was obtained for $n_L = 0.905 \pm 0.025$ and $A_0 = 2.325 \pm 0.238 \times 10^{13}$ Pa. The errors associated to A_0 and n_L were determined by sensitivity tests, where the values of n_L and A_0 were changed until the fit became visually unacceptable, which happened for a 10% increase of the SAE.

Using these parameters, the following relationship (eq 7) was used to describe the liquid–vapor equilibrium of HCHO solutions in water

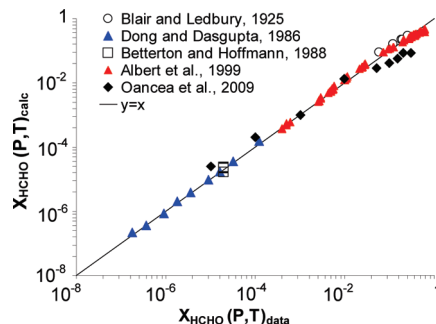


Figure 2. Comparison of experimental data $X_{\text{HCHO}}(P,T)_{\text{data}}$ with calculated values $X_{\text{HCHO}}(P,T)_{\text{calc}}$ using eq 7.

$$P_{\text{HCHO}}(X_{\text{HCHO}}, T) = (X_{\text{HCHO}})^{0.905} 2.325 \times 10^{13} \exp\left(-\frac{60.3 \times 10^3}{RT}\right) \quad (7)$$

where P_{HCHO} is the partial pressure of HCHO expressed in Pa, X_{HCHO} is the molar fraction of HCHO in the liquid solution, R is the gas constant, and T is the temperature in Kelvin.

Validation. Figure 2 shows that calculated and measured values of $X_{\text{HCHO}}(P,T)$ are in good agreement over an X_{HCHO} range covering more than 6 orders of magnitude, with T ranging from 278 to 423 K. The largest discrepancies were encountered with the data of Oancea et al.²⁵ with a difference between calculated and measured values varying monotonically from +130% at low concentrations to -70% at high concentrations. For the others studies, the deviations from eq 7 were below 50% with no systematic trend.

The introduction of the vapor depression factor n_L therefore appears to be an excellent way to calculate the HCHO partial pressure at thermodynamic equilibrium. Moreover this formulation also allows the calculation of the H_2O partial pressure, using eq 3. We can therefore calculate the total vapor pressure $P_{\text{tot}} = P_{\text{H}_2\text{O}} + P_{\text{HCHO}}$ in the gas phase at thermodynamic equilibrium, using eqs 3 and 7. This total pressure was measured by Oancea et al.²⁵ and Brandani et al.³³ by allowing a liquid solution of HCHO to equilibrate in a vacuum chamber. We compared their experimental data with the total vapor pressure calculated using our thermodynamic parameters. As shown in Figure 3, the total pressure decrease with increasing X_{HCHO} is well reproduced by our calculations for temperatures under 333 K. For higher temperatures, slight deviations appear especially for molar fractions over 0.2 where the temperature dependence of the activity and fugacity coefficients³³ should be taken into account. As we focus here on atmospheric applications of the vapor–liquid equilibrium where HCHO concentrations do not reach such high values, we did not perform further calculation and we recommend to use eqs 3 and 7 as a convenient and accurate formulation of vapor–liquid equilibrium for HCHO liquid solutions in the temperature and concentration ranges of atmospheric relevance.

Thermodynamics of the Solid Solution

To determine the thermodynamic coefficients of the solid–vapor equilibrium of HCHO and H_2O , the solubility of HCHO in ice was measured at different temperatures and partial pressures of HCHO. Experiments consisted in exposing large ice single crystals to known P_{HCHO} so that HCHO diffuses in ice. After several weeks of diffusion, ice crystals were analyzed to obtain the diffusion profile of HCHO, yielding both the solubility and the diffusion coefficient D_{HCHO} of HCHO in ice.

The experimental methods were adapted from those of Thibert and Domine^{31,32,34} who measured the diffusion coefficient and

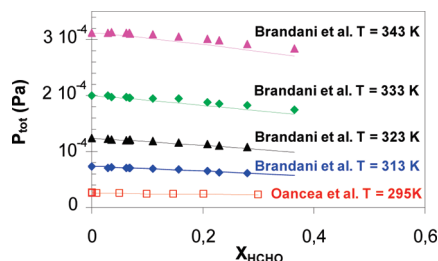


Figure 3. Equilibrium total vapor pressure ($P_{\text{H}_2\text{O}} + P_{\text{HCHO}}$) as a function of the HCHO molar fraction in the aqueous solution. Solid lines are calculations using eqs 3 and 7.

the solubility of HCl and HNO_3 in ice. The methods used for HCHO were described in the preliminary work of Perrier et al.¹⁴ but some improvements were necessary to allow the determination of these parameters at partial pressures closer to atmospheric conditions. A summary of the methods employed is reported here as well as the improvements that were developed for this study.

Experimental Methods to Study the H_2O –HCHO Solid Solution. Ice Crystal Growth. Ice single crystals were grown from ultrapure water delivered by a Millipore (Bedford, MA) Elix 35 system and subsequently purified by an Elga (High Wycombe Bucks, U.K.) Maxima HPLC system. The water was sampled when the total organic carbon level was below $5 \mu\text{g L}^{-1}$. Ice growth was achieved in a 0°C cold room by slowly freezing water over a seed crystal in a specific cylindrical crystallizer under a gradient of temperature to obtain cylindrical ice crystals of 8 cm in diameter and 10 cm long. A Peltier element that cooled the base of the crystallizer was used to control the growth rate that was always kept under 1 cm per day. Such a low speed allows ice to grow with a low density of defects. This method leads to ice crystals having c -axes normal to the axis of the cylinder. The total density of dislocations in ice crystals grown with our method was in the range 10^6 to 10^8 mm^{-3} .³⁵ One of the single ice crystal used during this study was analyzed by X-ray diffraction at the ESRF facility (Grenoble, France), which confirmed that the density of dislocations was lower than 10^8 mm^{-3} . This growth technique was preferred to the modified Bridgman method,³¹ which generates ice crystals with a higher density of dislocations. Each crystal used in doping experiments was controlled between crossed polaroids to confirm the orientation of the c -axis and the absence of visible small-angle boundary. A sample of each ice crystal was systematically analyzed for HCHO initial contamination before each doping experiment. Such a contamination never exceeded $X_{\text{HCHO}} = 3 \times 10^{-9}$.

Sample Machining. Crystals were cut in a cold room to a length of 4–5 cm, frozen onto a metal support, and lathed to a perfect cylindrical shape with a flat surface. One issue when machining ice is the formation of microcracks and appearance of small craters if the cutting procedure leads to high cutting forces. To minimize the formation of microcracks during lathing, ice crystals were machined with a low rotation speed ($150 \text{ revolutions min}^{-1}$) with a modified cutting tool. The cutting tool was shaped to get a very small negative cutting edge angle (less than 5°) and a high back rake angle (60°). This provides a very sharp cutting edge and minimal cutting forces.³⁶ The tool's depth of penetration never exceeded $100 \mu\text{m}$ and a finishing pass of $25 \mu\text{m}$ was performed to provide mirror machined surfaces.

Doping. The crystals were placed in a stainless steel diffusion chamber and exposed to the desired P_{HCHO} , which was obtained by flowing gas mixtures of HCHO diluted in nitrogen (Figure 4). The water saturation of the nitrogen at the temperature of

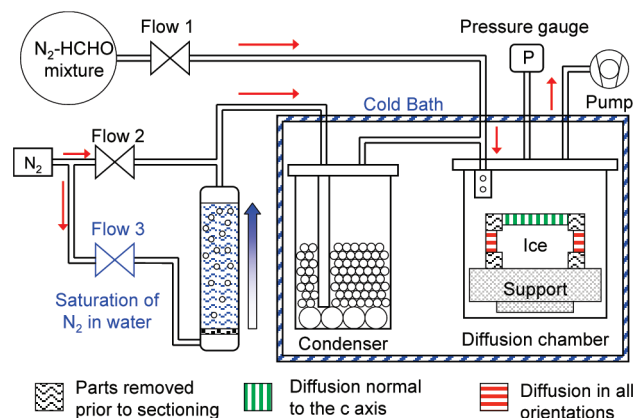


Figure 4. Experimental set up used to study the diffusion of HCHO in ice. The lathing procedure after diffusion is also indicated. Flow 2/Flow 3 is adjusted to obtain a water saturation of 110% at the temperature of the experiment. The excess water is trapped in the condenser.

the experiment was obtained by diluting a nitrogen flow saturated in water at ambient temperature (Flow 3) with dry nitrogen (Flow 2). Flow 2/Flow 3 was adjusted to obtain a water saturation of 110% at the temperature of the experiment, the excess water being trapped in the condenser. HCHO mixtures were prepared by heating paraformaldehyde to 140°C to generate pure gaseous HCHO that was diluted with nitrogen in 10 L glass bulbs. On the basis of the accuracy of the flow meters and manometer, we estimated that the uncertainty on P_{HCHO} when supplied to the ice crystal was 8%. The P_{HCHO} value and the chemical purity of the gas mixture were controlled at the outlet of the diffusion chamber by flowing the gas through a bubbler filled with water. Quantitative collection of HCHO in the bubbler was checked by placing a second bubbler in series. HCHO in water was analyzed by DNSAOA derivatization³⁷ and the derivative of the HCHO concentration with respect to time yielded the flux of HCHO and thus P_{HCHO} knowing the total gaseous flow. P_{HCHO} was as expected from the gas mixture, within the 8% uncertainty, once the lines were conditioned, which took 6 h. To ensure steady conditions from the beginning of the experiment, the gas lines were conditioned 12 h before each experiment with the desired HCHO and H_2O partial pressures.

Cutting Procedure. After a diffusion time of several weeks, serial sectioning of the doped crystals was performed on the lathe in the cold room, as detailed in Thibert and Domine.³¹ A first profile (normal to the c axis) was obtained by removing ice layers parallel to the flat surface of the cylinder. A second profile (a mixture of all crystallographic orientations) was obtained by removing concentric layers on the side of the cylinder. To maximize the accuracy on D_{HCHO} , the first layers sampled were $15 \mu\text{m}$ thick which yielded at least 4 points with a high X_{HCHO} . Such a thin sectioning was only possible by using the modified cutting tool. The shavings of each layer were recovered through a funnel designed to guide them into 20 mL borosilicated glass vials (Kimble Glass Inc., Vineland, NJ) mounted with PTFE/silicone-lined caps. The shavings of each layer were weighed and were generally in the range 40–150 mg. Vials were preliminarily washed with ultrapure water and residual water was evaporated under a warm flux of ultrapure nitrogen generated with a liquid nitrogen evaporator.

Analysis. Shavings melted in 20 mL vials were first diluted with $150 \mu\text{L}$ of ultrapure water. The resulting mixture was then transferred in $400 \mu\text{L}$ glass vials. This procedure allows a complete recovery of the shavings with minimal contamination

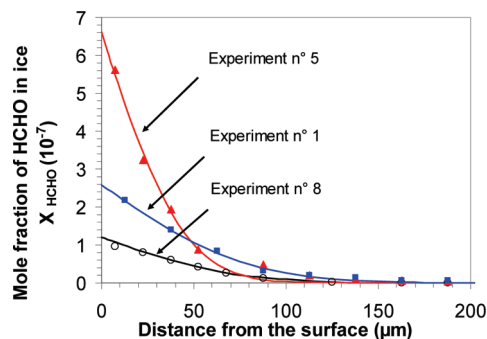


Figure 5. Typical experimental diffusion profiles of gaseous HCHO in ice single crystals. Concentrations are corrected from the blanks. Experimental conditions are detailed in Table 1. Lines are the fit of data to eq 8.

and dilution. Samples were analyzed using DNSAOA derivatization with fluorescence detection.³⁷ Typically 200 μL of a diluted solution of DNSAOA were added to perform the derivatization reaction. A 5 μL of sample was then injected in the HPLC system. More details on the analytical procedure can be found in Houdier et al.³⁷

Diffusion Profiles. Diffusion profiles corrected from the blanks were fitted to eq 8 (Figure 5), which is the solution to Fick's laws of diffusion in a semi-infinite solid with a constant supply of the diffusing species³⁸

$$X_{\text{HCHO}}(x, t) = X_{\text{HCHO}}^0(T, P_{\text{HCHO}}) \left[1 - \text{erf} \left(\frac{x}{2\sqrt{D_{\text{HCHO}}t}} \right) \right] \quad (8)$$

In eq 8, $X_{\text{HCHO}}(x, t)$ is the mole fraction of HCHO at a distance x from the diffusion interface after a diffusion time t . X_{HCHO}^0 is the mole fraction at the interface and therefore corresponds to the equilibrium solubility of HCHO in ice which depends on T and P_{HCHO} . D_{HCHO} is the diffusion coefficient of HCHO in ice which may depend on temperature, and erf is the error function.

Some diffusion profiles showed a deviation from eq 8 for $x > 100 \mu\text{m}$. This deviation at long distances has already been observed for the diffusion of HCl and HNO_3 in ice by Thibert et Domine^{31,32} and is typical of diffusion in defects that act as diffusion short circuits.³⁸ Thus, eq 8 was only applied to the

first part of the diffusion profiles where the influence of diffusion through the defects is negligible.

Experimental Difficulties. Obtaining a diffusion profile involves several experimental steps with their own intrinsic difficulties. Some of these difficulties deserve discussion if one is interested in reproducing this kind of experiments.

The major difficulty was to prevent any change in the ice crystal shape during the doping procedure. When exposing ice crystal to a gaseous flux for weeks, the ice crystal is prone to sublimation if the gaseous flux does not fulfill the exact saturating water pressure of ice at the experiment temperature. The ratio Flow2/Flow3 was adjusted so that the nitrogen water content was slightly above the saturation vapor pressure of ice and the excess water was condensed in a stainless steel condenser packed with stainless steel balls (Figure 4). Although this method is very accurate to control $P_{\text{H}_2\text{O}}$, we sometimes observed sublimation on some parts of the side of the cylinder. From a perfect cylinder shape, the ice crystal was evolving toward an oval shape with the c -axis of the ice lattice as one of the axis of the oval which indicates that sublimation occurred preferentially in one of the basal or prism face of ice. The causes of this modification are beyond the scope of this work, but it may be related to the anisotropy in growth and sublimation rates between prism and basal faces of ice crystals^{39,40} and in a possible difference in the saturating vapor pressure of water between basal and prism faces.

This change during the doping procedure was observed at -7 and -15 $^\circ\text{C}$ with a maximum difference between the two axes of the projected ellipse of about 100 μm for experiment 7. When lathing such oval cylinders, the depth $x = 0$ corresponds to the radius of the major axis. The recovered layers are therefore a mixture of several depths from the diffusion interface and the fit to the equation of diffusion leads to an overestimation of D_{HCHO} , although the value for solubility at the interface is not affected.

For each experiment, we attributed a quality index for the doping, cutting, and analysis of samples. The quality indices reported in Table 1 is the sum of 3 independent indexes ranging from 0 to 5, the highest values corresponding to the best confidence on the data. We evaluated the doping index by monitoring the stability of the gas flows and by inspecting the amount of hoar in the condenser. The cutting procedure was crucial and its associated quality index was carefully determined for each experiment. The main difficulty lies with the recovery

TABLE 1: Experimental Results for the Diffusion of Gaseous HCHO in Ice between -7 and -30 $^\circ\text{C}$

| exp. no. | orientation | T ($^\circ\text{C}$) | P_{HCHO} (10^{-3} Pa) | t_{diff} (10^6 s) | X_{HCHO} (10^{-8} mole frac) | D_{HCHO} (10^{-12} $\text{cm}^2 \text{s}^{-1}$) | quality (over 15) |
|----------------|-------------|-----------------------------|--------------------------------------|----------------------------------|---|---|----------------------|
| 1 ^a | face | -15 | 17 | 0.77 | 26.1 | 23.4 | 10 |
| 2 ^a | face | -15 | 17 | 0.92 | 32.0 | 23.0 | 8 |
| 3 | face | -15 | 50 | 0.92 | 61.6 | 13.9 | 9 |
| 4 | face | -15 | 5.3 | 1.18 | 13.2 | 4.70 | 9 |
| 5 | face | -7 | 101 | 0.93 | 77.3 | 6.67 | 11 |
| 5 ^a | side | -7 | 101 | 0.93 | 75.6 | 23.7 | 11 |
| 6 ^a | face | -7 | 2.1 | 0.93 | 3.36 | 41.0 | 12 |
| 6 ^a | side | -7 | 2.1 | 0.93 | 3.24 | 41.8 | 12 |
| 7 ^a | face | -7 | 20 | 1.81 | 14.6 | 17.8 | 10 |
| 7 ^a | side | -7 | 20 | 1.81 | 15.0 | 53.0 | 10 |
| 8 | face | -30 | 2.0 | 2.00 | 12.0 | 5.66 | 14 |
| 8 | side | -30 | 2.0 | 2.00 | 13.5 | 7.62 | 14 |
| 9 | face | -30 | 20 | 1.14 | 77.8 | 3.86 | 12 |
| 10 | face | -30 | 0.35 | 0.83 | 3.06 | 6.70 | 15 |
| 10 | side | -30 | 0.35 | 0.83 | 3.00 | 7.70 | 15 |

^a Experiments where sublimation during the doping procedure lead to a large positive artifact in the determination of D_{HCHO} .

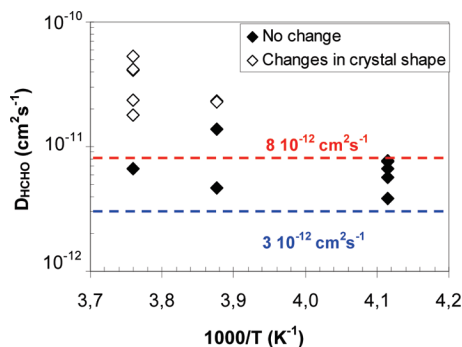


Figure 6. Arrhenius plot of the diffusion coefficient of HCHO in ice, D_{HCHO} . Open diamonds indicate experiments where a large positive artifact in D_{HCHO} was caused by partial sublimation of the ice crystal.

of the first layer, which required to slowly approach the cutting tool to the ice crystal until contact. When the first shaving started to form, the digital readout was set to 0 μm and all subsequent cutting depths were based on this absolute reference. The comparison between the recovered and expected mass of shavings for each layer was used to detect any bias in the cutting of the first layer. A lower mass for the first layer indicated an incomplete recovery of shavings, which lowered the cutting procedure index. The quality of the chemical analysis was estimated by blanks analysis and calibrations consistency. Because melted samples were prone to contamination, water blanks were prepared along with the samples. Typically, six blanks were analyzed and we used both the mean value and the standard deviation to attribute the chemical analysis index. Dispersion in blanks values or blanks above 0.5 ppbw lowered this quality index.

We performed 13 experiments among which 3 were discarded because their quality index was less than 8.

Results on the H_2O –HCHO Solid Solution. A total of 10 successful diffusion experiments were performed under various conditions of temperature (from -7 to -30 $^{\circ}\text{C}$) and P_{HCHO} (from 3.48×10^{-4} to 0.1 Pa). Details of each experiment are listed in Table 1. When diffusion was measured in both surfaces of the cylinder (flat face and side), we obtained two independent measurements of the solubility. Both measurements differ from each other by 5% on average which supports the reliability of our solubility results.

Kinetics of Diffusion. The diffusion coefficients we measured are very low and around $10^{-12} \text{ cm}^2 \text{ s}^{-1}$, which is of the same order as the diffusion coefficients of HCl in ice.³¹ The scatter in the values reported in Table 1 is quite broad with values between 3.9 and $53 \times 10^{-12} \text{ cm}^2 \text{ s}^{-1}$. These D_{HCHO} values must be considered as upper limits since the presence of diffusion short circuits affects the calculated values.³² As detailed in the experimental methods, another factor that caused the overestimation of D_{HCHO} is the change in ice crystal shape because of sublimation processes during the doping procedure (see Table 1). The resulting large scatter (Figure 6) makes it impossible to detect a temperature dependence of D_{HCHO} . However we estimate that the true values of D_{HCHO} in the -7 to -30 $^{\circ}\text{C}$ range are in range 3 to $8 \times 10^{-12} \text{ cm}^2 \text{ s}^{-1}$. This D_{HCHO} range does not include the value obtained during experiment 3 because the diffusion profile showed a very large deviation from eq 8, indicating that the amount of defects in the single ice crystal was much higher than in the other experiments.

Thermodynamics. As done for the liquid solution, the solubility of HCHO in ice can be described by the following relationship (eq 9)

$$P_{\text{HCHO}}(X_{\text{HCHO}}, T) = (X_{\text{HCHO}})^{n_s} A'_0 \exp\left(-\frac{\Delta h_{\text{sub}}}{RT}\right) \quad (9)$$

where Δh_{sub} is the partial molar enthalpy of sublimation of HCHO, A'_0 a constant (in Pa) for the ice–HCHO system and n_s is the ice vapor depression factor. Our data have been analyzed using two methods to determine the values of the thermodynamic parameters in eq 9.

1. Determination of n_s , A'_0 and Δh_{sub} from Two Separate Linear Regressions. To test whether our data follow eq 9, two separate linear regressions were performed. Given the range of HCHO concentrations we measured in ice, HCHO can be considered at infinite dilution and n_s can be considered independent of composition. This hypothesis was confirmed by our data where $\log X_{\text{HCHO}}$ was found to be a linear function of $\log P_{\text{HCHO}}$ whose slope is $1/n_s$ (Figure 7).

The calculated values for n_s are similar for -7 and -30 $^{\circ}\text{C}$ with respectively $n_s = 1.246 \pm 0.025$ and $n_s = 1.243 \pm 0.074$. This parameter n_s also has to be considered independent of temperature despite experiments performed at -15 $^{\circ}\text{C}$ yielding a significantly higher value of $n_s = 1.457 \pm 0.135$. These experiments at -15 $^{\circ}\text{C}$ were the first that we performed and appear less reliable than those at -7 and -30 $^{\circ}\text{C}$ because of higher uncertainties during the lathing procedure that require substantial machining skills. Since the P_{HCHO} range is larger for -7 and -30 $^{\circ}\text{C}$ and because we have a higher confidence in these latter experiments, we can reasonably consider that the higher value for n_s at -15 $^{\circ}\text{C}$ is due to the addition of analytical errors and lathing uncertainties. For the following we will consider the mean value of n_s at -7 and -30 $^{\circ}\text{C}$ which is $n_s = 1.245 \pm 0.05$.

The partial molar enthalpy of sublimation of HCHO is also assumed to be independent of temperature and has been calculated using $n_s = 1.245$. From eq 9 it appears that $\ln(P_{\text{HCHO}}/X_{\text{HCHO}}^{n_s})$ is a linear function of inverse temperature whose slope

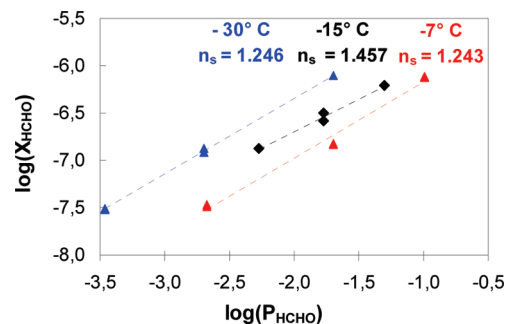


Figure 7. Equilibrium solubility of HCHO in ice as a function of the partial pressure of HCHO P_{HCHO} . For each temperature, the data have been fitted to eq 9.

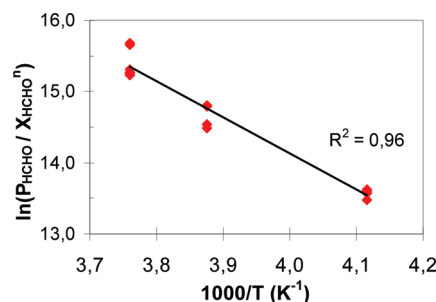


Figure 8. Arrhenius plot of $P_{\text{HCHO}}/X_{\text{HCHO}}^{n_s}$. The slope of the fit is equal to $\Delta h_{\text{sub}}/R$ and the y-intercept is equal to $\ln(A'_0, \text{Pa})$ yielding $\Delta h_{\text{sub}} = 42.15 \text{ kJ/mol}$ and $A'_0 = 8.82 \times 10^{14} \text{ Pa}$.

TABLE 2: Determination of the Three Parameters A'_0 , Δh_{sub} , and n_S According to the Two Methods^a

| | n_S | Δh_{sub} (kJ/mol) | $\ln(A'_0, \text{Pa})$ |
|---------------------------------|------------------|----------------------------------|------------------------|
| two separate linear regressions | 1.245 ± 0.05 | 42.15 ± 2.38 | 34.41 ± 1.12 |
| three-variables method | 1.246 | 43.2 | 34.95 |

^a Values calculated with the second method are in the uncertainty range of the first method.

is $-\Delta h_{\text{sub}}/R$ and the y-intercept is $\ln(A'_0)$. The Arrhenius plot of $P_{\text{HCHO}}/X_{\text{HCHO}}^{n_S}$ (Figure 7) yields $\Delta h_{\text{sub}} = 42.15 \pm 2.38$ kJ/mol and $\ln(A'_0, \text{Pa}) = 34.41 \pm 1.12$.

2. *Three-Variables Least-Squares Method.* As already proposed for the study of HCl and HNO₃ solid solutions,^{31,32} a three-variables least-squares method has been used to determine simultaneously the three parameters A'_0 , Δh_{sub} and n_S . We have not calculated the errors on the parameters determined with this method. Results of calculations are reported in Table 2 and compare well with those obtained by separate linear regressions. Both sets of values are in very good agreement and yield a calculated solubility within the experimental error of the data with a mean deviation of less than 10%.

Since the first method provides the uncertainties of the three parameters, the pressure and temperature dependences for the solubility calculated by the first method will be used subsequently according to the following relationship (eq 10) with T in K, P_{HCHO} in Pa and X_{HCHO} the mole fraction of HCHO in ice

$$X_{\text{HCHO}} = 9.898 \times 10^{-13} e^{(4072/T)} (P_{\text{HCHO}})^{1/1.245} \quad (10)$$

The value of Δh_{sub} is 30% lower than Δh_{vap} (60.3 kJ mol⁻¹) which indicates a lower energy release when HCHO is dissolved in ice rather than in liquid water. The same trend was observed for HCl and HNO₃ solid solutions in ice,^{31,32} although the differences were lower (16% for HCl and 11% for HNO₃). The lower energy release by the formation of a solid solution is probably due to the lower mobility of H₂O molecules in the ice phase, which prevents the solute from finding the optimal configuration in the solid. In the case of HCHO, we speculate that the higher difference between Δh_{sub} and Δh_{vap} might be

due to the formation of polyoxomethylene glycols in the liquid phase (R1 and R2) which helps to diminish the enthalpy of HCHO in liquid solution. In ice, the low concentrations of HCHO and the lower solute mobility doubtless considerably reduce the probability of polyoxomethylene glycols formation, explaining the low Δh_{sub} value, relative to Δh_{vap} .

H₂O–HCHO Phase Diagram

The binary system H₂O–HCHO has been studied since the early of the 1930s but synthesis of these studies was only achieved by Sobolova et al.²⁷ who proposed the temperature–composition phase diagram in the mid 1980s. We propose in this study to construct the P_{HCHO} versus $1/T$ phase diagram that is more useful for atmospheric applications.

Construction of the $P_{\text{HCHO}}-1/T$ Phase Diagram. The first step in the construction of the $P_{\text{HCHO}}-1/T$ phase diagram is to determine the boundaries between the different phases (liquid, ice, and solid polymers). In the $P_{\text{HCHO}}-1/T$ phase diagram, the boundary between the liquid phase and the solid phase is obtained by plotting the partial pressure P_{HCHO} as a function of the melting temperature of the solid phase $T_{\text{melt}}(X_{\text{HCHO}})$ (Figure 9). Soboleva et al.²⁷ provide the melting temperature $T_{\text{melt}}(X_{\text{HCHO}})$ for mixtures over a HCHO concentration range from $X_{\text{HCHO}} = 0$ (pure ice) to $X_{\text{HCHO}} = 0.9$. For concentrations lower than the eutectic composition at $X_{\text{HCHO}} = 0.195$, the solid phase in equilibrium with the liquid solution is ice. For higher concentrations, the solid phase is a mixture of solid polyoxomethylene glycols. We calculated the partial pressure of formaldehyde at the melting temperature $P_{\text{HCHO}}(T_{\text{melt}})$ by using eq 7 which describes the vapor–liquid equilibrium.

We also plotted isosolubility curves in this phase diagram. The consequence of eqs 4 and 8 is that isosolubility curves in this phase diagram are straight lines with slopes equal to $-\Delta h_{\text{vap}}/R$ for the liquid solution, and $-\Delta h_{\text{sub}}/R$ for the solid solution. Those lines have been calculated for molar fractions in the liquid phase from $X_{\text{HCHO}} = 2 \times 10^{-7}$ to the eutectic composition $X_{\text{HCHO}} = 0.195$. For solid solutions, solubility is lower and isosolubility lines are plotted for the X_{HCHO} range 1×10^{-9} to 3×10^{-6} .

As there is no thermodynamic study available for the polyoxomethylene glycols, we assumed that the boundary between the solid polymers and the ice solid solutions is

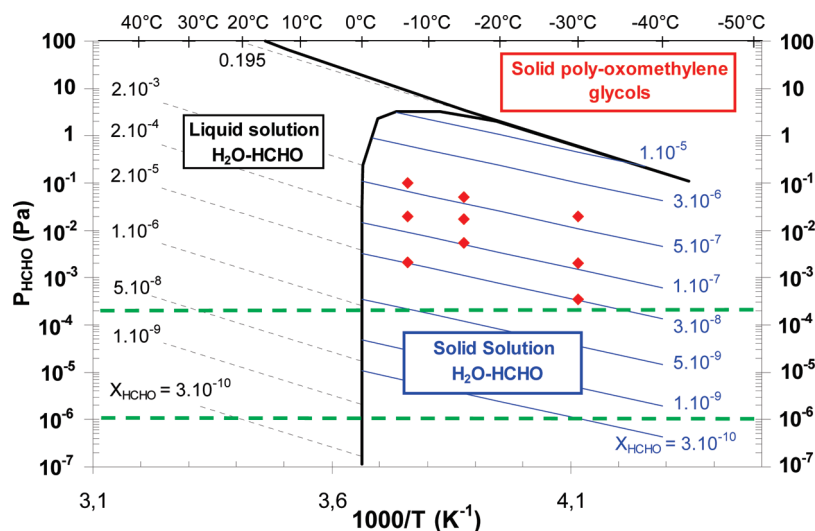


Figure 9. Pressure-inverse temperature phase diagram with isosolubility curves of HCHO in ice (calculated from eq 10) and aqueous solutions (calculated from eq 7). The red diamonds indicate the conditions of our experiments. The green dashed lines represent the typical atmospheric P_{HCHO} range.

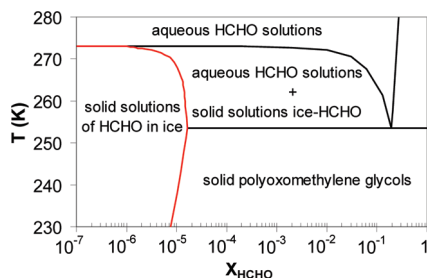


Figure 10. Temperature–composition phase diagram (logarithmic scale). Black lines are the liquidus and eutectic lines. The red line is the solidus line calculated from our data.

described by the isosolubility line of the eutectic composition. This hypothesis is similar to the one made for the boundary between the hydrates involved in HNO_3 and HCl solid solutions.^{31,32}

In the atmosphere, the P_{HCHO} range is quite broad. Values in the range 5 to 50×10^{-6} Pa for pristine air have been measured in polar regions^{15,16,41,42} but P_{HCHO} can reach values as high as 1 to 2×10^{-4} Pa in the firm^{15,41} and over oceans.⁴³ Extremes values of P_{HCHO} up to 10^{-2} Pa were measured but are only marginally relevant because they correspond to highly polluted regions such as suburban areas.^{2,44–47} In Figure 9, we indicated by dashed green lines the P_{HCHO} range 10^{-6} to 2×10^{-4} Pa, which corresponds to typical concentrations for pristine to moderately polluted areas.

Solidus. As there was no study available on solid solutions when Soboleva et al.²⁷ published their temperature–composition phase diagram, they considered that the solidus was a straight line at the melting temperature of pure ice, implicitly assuming that the solubility of HCHO in ice is zero. Such an approximation is reasonable for a number of applications but absolutely not for the atmosphere. Using our results, we calculated the composition of the condensed phase along the melting temperature curve and thus add the solidus to the temperature–composition phase diagram (Figure 10). We also reported the boundary between solid polyoxomethylene glycols and the solid solution of HCHO in ice that was calculated from the concentrations in the ice solid solutions at the boundary with polyoxomethylene glycols (see Figure 9). Again, this latter boundary should be considered as an approximate calculation, because thermodynamics of solid poly oxomethylene glycols are not known.

Partition Coefficient. In the domain where aqueous and solid solution of HCHO coexist (Figure 10), the composition of ice is in equilibrium with the liquid solution according to the ice–water partition coefficient K . K is the ratio between the HCHO composition of the solid solution X_{ice} and the composition of the liquid solution X_{liq} in equilibrium at the melting temperature: $K = X_{\text{ice}}/X_{\text{liq}}$. The experimental measurement of such a coefficient by growing ice in a liquid solution is very difficult to obtain because of artifacts and nonequilibrium processes occurring during crystal growth.³¹ It is therefore more reliable to calculate K values from properties of the liquid and solid solutions measured independently. As shown in the P_{HCHO} , $1/T$ phase diagram (Figure 9), the solubility of HCHO is orders of magnitude lower in ice solid solutions than in liquid solutions. Figure 11 is a plot of the calculated values of K which shows a monotonic decrease from 10^{-3} to 8×10^{-5} with decreasing melting temperatures and therefore increasing HCHO concentrations. These values are in the same range as those calculated for the ice–water partitioning of HCl ³¹ but are higher than for HNO_3 which is much less soluble in ice than in water solutions.³²

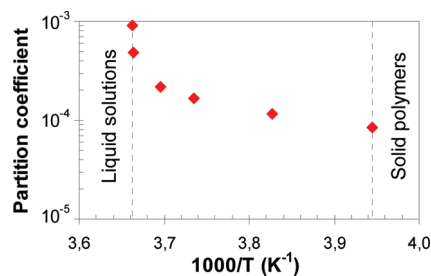


Figure 11. Calculated partition coefficient $K = X_{\text{ice}}/X_{\text{liq}}$ versus temperature. Dashed lines are the ice–liquid solutions and ice–solid polyoxomethylene glycols boundaries.

Discussion

Since we have not added new experimental data to the liquid–vapor equilibrium of the H_2O –HCHO system, this discussion will only focus on the results obtained for the solid solution of formaldehyde in ice.

Comparison with Previous Data. To our knowledge, the only available experimental studies on the partitioning of HCHO between the gas phase and ice are those of Burkhart et al.²⁶ and Perrier et al.¹⁴

Although our study is based on the same experimental setup as that used by Perrier et al., we obtained significantly different results. At -15 °C and for $P_{\text{HCHO}} = 1.7 \times 10^{-2}$ and 3.4×10^{-2} , they calculated $X_{\text{HCHO}} = 5.4 \times 10^{-7}$ and 9.0×10^{-7} whereas our results are $X_{\text{HCHO}} = 1.7 \times 10^{-7}$ and 2.9×10^{-7} , respectively. One possible reason to explain their 3 times as large solubility is contamination during their lathing and analytical procedures. Indeed, when analyzing layers in which HCHO had not diffused, they found $X_{\text{HCHO}} = 3 \times 10^{-8}$, which was higher than their ice blanks. Such contamination can produce strong overestimation of solubility, especially when shavings are very diluted for analysis. For comparison, our diffusion profile obtained during experiment 10 had a maximum concentration of $X_{\text{HCHO}} = 3 \times 10^{-8}$, which corresponds to the blanks of Perrier et al. whereas our blanks for this experiments had a value of 1.2×10^{-9} . They obtained diffusion coefficients between 38 and 500×10^{-12} $\text{cm}^2 \text{s}^{-1}$, which barely overlap our highest values and remain 10 times higher than our lowest values. It is worth noting that their lathing procedure led to the formation of microcracks in ice and thus to higher densities of defects in ice. Such defects act as diffusion short-circuits and therefore yield higher apparent D_{HCHO} .³⁸

Burkhart et al.'s exposed homemade “snow”, which consisted in a mixture of spherical ice grains of ~ 100 μm in diameter obtained by freezing water droplets into liquid nitrogen, to a known partial pressure of HCHO at temperatures between -5 and -35 °C. They calculated partition coefficients K_d defined as the ratio between the concentration of HCHO in snow C_{HCHO} and the partial pressure P_{HCHO} : $K_d = C_{\text{HCHO}}/P_{\text{HCHO}}$ with C_{HCHO} in mol/L and P_{HCHO} in atm. This formulation assumes that the solubility is a linear function of the partial pressure ($n_s = 1$), which is not the case since we measured $n_s = 1.245 \pm 0.05$. However we can compare their results to concentrations at equilibrium calculated by eq 10 for their experimental conditions. We found that on average, their concentrations are about half the concentrations at thermodynamic equilibrium derived from our work.

The authors assumed that the equilibrium was not completely reached for the experiments at -35 °C. In Figure 12, we report the calculated ratio between Burkhart et al.'s concentrations and the expected concentrations at equilibrium (eq 10) for P_{HCHO}

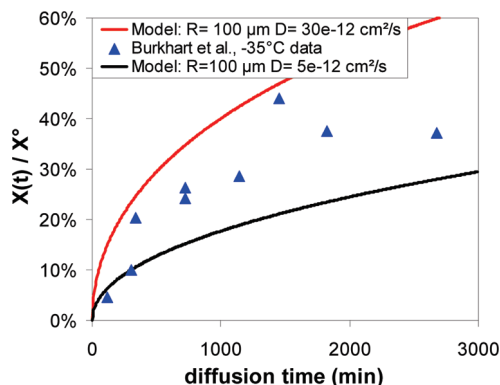


Figure 12. Ratio between the concentrations reported by Burkhardt et al. at $-35\text{ }^{\circ}\text{C}$ $X(t)$ and the concentrations X^0 calculated by eq 10 as a function of diffusion time. The solid lines have been calculated by a diffusion model in ice spheres for two values of D_{HCHO} .

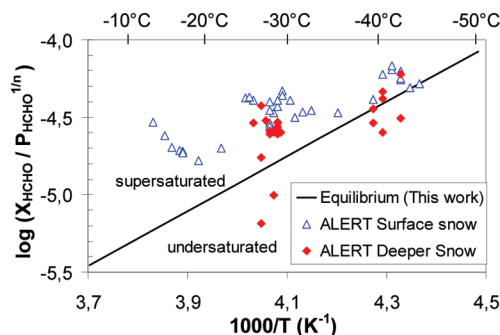


Figure 13. Arrhenius plot of $X_{\text{HCHO}}/P_{\text{HCHO}}^{1/n}$. Snow surface layers are differentiated from the rest of the snowpack.

used in their experiments at $-35\text{ }^{\circ}\text{C}$ as a function of time. We also plotted the evolution of concentration in a spherical grain of $100\text{ }\mu\text{m}$ calculated by a numerical model of diffusion using a Crank–Nicolson scheme.⁴⁸ As shown in Figure 12, the ratio between the concentrations X^0 calculated by eq 10 and $X(t)$ measured by Burkhardt et al. is in good agreement with the ratio to the equilibrium calculated by the diffusion model for D_{HCHO} in the range $5\text{ to }30 \times 10^{-12}\text{ cm}^2\text{ s}^{-1}$. This D_{HCHO} range contains a value higher than those we recommend ($3\text{ to }8 \times 10^{-12}\text{ cm}^2\text{ s}^{-1}$), however it is known that the amount of defects generated when freezing water in liquid nitrogen can produce an apparent diffusion coefficient greater by a factor of at least 100 than the true value.⁴⁹ We therefore believe that the concentrations reported by Burkhardt et al.²⁶ correspond to 40–50% of the concentrations at thermodynamic equilibrium because the duration of their experiments was not sufficient to reach equilibrium.

Atmospheric Applications. Partitioning of HCHO in the High Arctic. We can now compare our results to the partitioning of HCHO observed between the atmospheric boundary layer and the snow during the ALERT2000 field campaign,^{13,16} which took place at Alert (Canadian High Arctic, $82^{\circ}30'\text{ N}$). During that campaign, daily snow samples were collected for HCHO chemical analysis and P_{HCHO} was also measured with an hourly resolution. Snow physical properties such as specific surface area (SSA), density, and temperature were also measured.

From those data, we can calculate a partition coefficient $X_{\text{HCHO}}/P_{\text{HCHO}}^{1/n}$ with $n = 1.245$. At thermodynamic equilibrium, this variable is a linear function of inverse temperature with an associated slope of $\Delta h_{\text{sub}}/nR$. In Figure 13, we compare the equilibrium partitioning line calculated from this study (eq 10) to the values calculated from the Alert data. We distinguish here the surface layer of snow resulting from the last snowfall

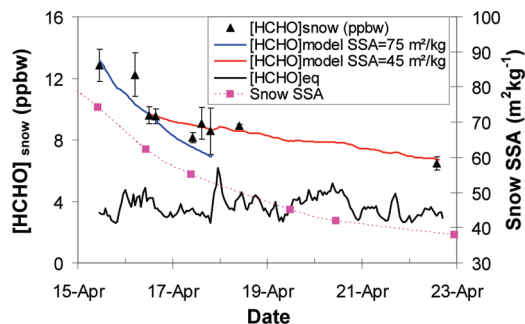


Figure 14. Measured and calculated [HCHO] for the April 14, 2000 snowfall. SSA is also reported. [HCHO] on April 14, 2000 was estimated to be 18 ppbw.

from deeper snow layers that were covered by a new layer at the sampling date. Because of the small accumulation rate at Alert, a layer 5 cm below the surface can be about one month old. More details on the snowpack studied can be found in Domine et al.⁵⁰ Values above the equilibrium line imply that the snow is supersaturated.

As shown in Figure 13, snow of surface layers is always supersaturated but a trend toward equilibration is observed and older snow layers are closer to the equilibrium especially for winter layers when snow temperature was around $-40\text{ }^{\circ}\text{C}$. This trend toward equilibration is confirmed in the following case study.

Solid State Diffusion As the Equilibration Process. As a case study for the HCHO decrease observed in fresh snow, we now consider the time-evolution of the snow layer fallen on April 14, 2000 whose HCHO concentration (in part per billion in weight, ppbw), temperature, and specific surface area (SSA, in $\text{m}^2\text{ kg}^{-1}$) were monitored on a daily basis for one week.¹³ As reported in Figure 14, HCHO concentrations show a fast decrease from 13 to 9 ppbw during the first two days following the snowfall, followed by a slow decrease to reach a value of 6.5 ppbw on April 22, 2000. We test here whether this decrease can be explained by the following scenario: (i) Snow is deposited during the snowfall at a concentration that is out of equilibrium because of atmospheric conditions during its formation different from those at the surface. (ii) After deposition, snow composition tends toward thermodynamic equilibrium by solid state diffusion of HCHO out of snow crystals. The snow crystals in the immediate vicinity of the ice–air interface is assumed to be at thermodynamic equilibrium with a concentration $[\text{HCHO}]_{\text{eq}}$ calculated using eq 10. Values of T and P_{HCHO} measured during the campaign were in the range $-42\text{ to }-12\text{ }^{\circ}\text{C}$ and 100 to 400 pptv. The adsorption of HCHO onto the surface of ice crystals is neglected. Indeed, using results of Collignon et al.⁵¹ and Winkler et al.,⁵² we calculated that adsorption of HCHO for the T and P_{HCHO} ranges encountered during the campaign accounts for no more than 0.03 ppbw.

In our diffusion model, snow crystals are treated as ice spheres whose equivalent diameter (d) is calculated from the specific surface area of snow with $d = 6/(\rho_{\text{ice}}\text{ SSA})$, where ρ_{ice} is the density of ice (917 kg m^{-3} at $0\text{ }^{\circ}\text{C}$). Because of metamorphism, snow SSA decreased from $84\text{ m}^2\text{ kg}^{-1}$ on April 14 to $38\text{ m}^2\text{ kg}^{-1}$ on April 22, resulting in equivalent diameters of 75 and $160\text{ }\mu\text{m}$, respectively. Our model is at this stage not able to take into account the modification of the grain size with time. We therefore performed two calculations with a static interface using SSAs of 75 and $45\text{ m}^2\text{ kg}^{-1}$, which are assumed to be representative of snow for the time periods April 14–17 and April 17–23, respectively.

Our model needs to be initialized with the X_{HCHO} value at the moment of snow deposition, and this value is assumed to be spatially homogeneous within a snow crystal. Since the snow was not analyzed when it fell on April 14 and because the value of D_{HCHO} is not exactly known (Figure 6), several calculations were performed with D_{HCHO} in the range 3 to $8 \times 10^{-12} \text{ cm}^2 \text{ s}^{-1}$ and snow initial concentrations in the range 14 ppbw (value on April 15) to 24 ppbw which is, to our knowledge, the highest value ever measured for a fresh snowfall in the arctic.¹⁵ The best fit to observations was obtained for an initial concentration of 18 ppbw and $D_{\text{HCHO}} = 6 \times 10^{-12} \text{ cm}^2 \text{ s}^{-1}$. This latter value is very close to the mean of our recommended range (Figure 6).

As shown in Figure 14, the fast HCHO decrease observed during April 15–17 is well reproduced by our calculation with $\text{SSA} = 75 \text{ m}^2 \text{ kg}^{-1}$. The slow decrease observed during April 17–23 is well reproduced by the calculation with $\text{SSA} = 45 \text{ m}^2 \text{ kg}^{-1}$. The hypothesis that snow is equilibrating with the atmosphere by diffusion of HCHO in the ice lattice of snow crystals therefore appears consistent with observations as well as the influence of the SSA on the rate of equilibration. This case study shows that a typical snowfall at Alert took several weeks to equilibrate with the atmosphere. Our explanation of Figure 13, showing that fresh snow is always supersaturated is therefore that (1) falling snow was always supersaturated because of different conditions in the cloud where the snow formed; and (2) equilibration was slow because it is governed by solid state diffusion, and the snow was not yet equilibrated, even 9 days after the snow fall.

Although our simplified model has to be considered as a preliminary approach, it emphasizes the importance of complementing the interpretation of snow composition with measurements of its physical properties such as SSA since this variable affects the rate of equilibration of snow crystals with the atmosphere.

Conclusion

The work presented here proposes formulations of the thermodynamic equilibrium of HCHO between the gas phase, liquid water, and ice. For liquid solutions of HCHO in water, we pointed out the lack of internal consistency of Henry's law coefficients, which depend on the concentration of the liquid phase. The formulation we propose here accurately describes the existing data for the vapor–liquid equilibrium. We believe that similar formulations probably apply to other organics of atmospheric interest and that the frequent use of Henry's law coefficients should be reconsidered. The study of the solubility and diffusion of HCHO in ice yielded new results on the equilibrium of HCHO in ice. The partial pressure versus inverse temperature phase diagram for the H_2O –HCHO system was drawn in the light of our results. The ice/water partition coefficient was also calculated, as well as the solidus line that complements the existing temperature–composition phase diagram established in the mid 1980s.

The kinetics of diffusion of HCHO in ice was shown to be a very slow process. It needs to be considered to understand the HCHO concentrations measured in snow and in the atmosphere. Existing laboratory and field measurements were analyzed in light of our results and lead to the conclusion that deviations from thermodynamic equilibrium are consistent with the kinetics of diffusion that also depend on snow physical properties, essentially the specific surface area. We therefore emphasize the critical importance of measuring snow physical properties to quantify HCHO exchanges between the snowpack and the atmospheric boundary layer.

Acknowledgment. This work was supported by the LEFE-CHAT program of CNRS-INSU and Université Joseph Fourier of Grenoble. We thank Maurine Montagnat for the X-ray analysis at the ESRF facility, Laura Capolo for her help in growing quality ice crystals, and Romain Duphil for his advice on lathing procedures and tool design.

References and Notes

- (1) Finlayson-Pitts, B.; Pitts, J. N., Jr. *Atmospheric Chemistry: Fundamentals and Experimental Techniques*; John Wiley & Sons Inc: New York, 1986.
- (2) Possanzini, M.; Palo, V. D.; Cecinato, A. *Atmos. Environ.* **2002**, *36*, 3195–3201.
- (3) Riedel, K. J. *Geophys. Res.* **2005**, *110*.
- (4) Carter, W. P. *Atmos. Environ., Part A* **1990**, *24*, 481–518.
- (5) Atkinson, R. *Atmos. Environ.* **2000**, *34*, 2063–2101.
- (6) Jacob, D. J. *Atmos. Environ.* **2000**, *34*, 2131–2159.
- (7) Munger, J. W.; Jacob, D. J.; Daube, B. C.; Horowitz, L. W.; Keene, W. C.; Heikes, B. G. *J. Geophys. Res.* **1995**, *100*, 9325–9333.
- (8) Kawamura, K.; Steinberg, S.; Kaplan, I. R. *Atmos. Environ.* **1996**, *30*, 1035–1052.
- (9) Largiuni, O.; Giacomelli, M. C.; Piccardi, G. J. *Atmos. Chem.* **2002**, *41*, 1–20.
- (10) Ervens, B.; Herckes, P.; Feingold, G.; Lee, T.; Collett, J. L.; Kreidenweis, S. M. *J. Atmos. Chem.* **2003**, *46*, 239–269.
- (11) Matsumoto, K.; Kawai, S.; Igawa, M. *Atmos. Environ.* **2005**, *39*, 7321–7329.
- (12) Ervens, B.; Gligorovski, S.; Herrmann, H. *Phys. Chem. Chem. Phys.* **2003**, *5*, 1811–1824.
- (13) Perrier, S.; Houdier, S.; Dominé, F.; Cabanes, A.; Legagneux, L.; Sumner, A. L.; Shepson, P. B. *Atmos. Environ.* **2002**, *36*, 2695–2705.
- (14) Perrier, S.; Sassini, P.; Dominé, F. *Can. J. Phys.* **2003**, *81*, 319–324.
- (15) Hutterli, M. A.; Röthlisberger, R.; Bales, R. C. *Geophys. Res. Lett.* **1999**, *26*, 1691–1694.
- (16) Sumner, A. L.; Shepson, P. B.; Grannas, A. M.; Bottenheim, J. W.; Anlauf, K. G.; Worthy, D.; Schroeder, W. H.; Steffen, A.; Dominé, F.; Perrier, S.; Houdier, S. *Atmos. Environ.* **2002**, *36*, 2553–2562.
- (17) Grannas, A. M.; Jones, A. E.; Dibb, J.; Ammann, M.; Anastasio, C.; Beine, H. J.; Bergin, M.; Bottenheim, J.; Boxe, C. S.; Carver, G.; Chen, G.; Crawford, J. H.; Dominé, F.; Frey, M. M.; Guzmán, M. I.; Heard, D. E.; Helmig, D.; Hoffmann, M. R.; Honrath, R. E.; Huey, L. G.; Hutterli, M.; Jacobi, H. W.; Klán, P.; Lefer, B.; McConnell, J.; Plane, J.; Sander, R.; Savarino, J.; Shepson, P. B.; Simpson, W. R.; Sodeau, J. R.; von Glasow, R.; Weller, R.; Wolff, E. W.; Zhu, T. *Atmos. Chem. Phys.* **2007**, *7*, 4329–4373.
- (18) Chen, G.; Huey, L.; Crawford, J.; Olson, J.; Hutterli, M.; Sjøstedt, S.; Tanner, D.; Dibb, J.; Lefer, B.; Blake, N.; Davis, D.; Stohl, A. *Atmos. Environ.* **2007**, *41*, 7806–7820.
- (19) Blair, E. W.; Ledbury, W. J. *Chem. Soc.* **1925**, *127*, 27–40.
- (20) Dong, S.; Dasgupta, P. K. *Environ. Sci. Technol.* **1986**, *20*, 637–640.
- (21) Betterton, E. A.; Hoffmann, M. R. *Environ. Sci. Technol.* **1988**, *22*, 1415–1418.
- (22) Albert, M.; Hahnenstein, I.; Hasse, H.; Maurer, G. *AIChE J.* **1996**, *42*, 1741–1752.
- (23) Albert, M.; Garcia, B. C.; Kreiter, C.; Maurer, G. *AIChE J.* **1999**, *45*, 2024–2033.
- (24) Seyfioglu, R.; Odabasi, M. *Environ. Monit. Assess.* **2007**, *128*, 343–349.
- (25) Oancea, A.; Hanoune, B.; Focsa, C.; Chazallon, B. *Environ. Sci. Technol.* **2009**, *43*, 435–440.
- (26) Burkhardt, J. F.; Hutterli, M. A.; Bales, R. C. *Atmos. Environ.* **2002**, *36*, 2157–2163.
- (27) Soboleva, O.; Blazhin, Y.; Ogorodnikov, S. *Zh. Prikl. Khim.* **1984**, *57*, 2290–2293.
- (28) Winkelman, J. G. M.; Voorwinde, O. K.; Ottens, M.; Beenackers, A. A. C. M.; Janssen, L. P. B. M. *Chem. Eng. Sci.* **2002**, *57*, 4067–4076.
- (29) Leicester, H. M.; Klickstein, H. S. *A Source Book in Chemistry, 1400–1900*; Harvard University Press: Cambridge, MA, 1969.
- (30) Hanson, D.; Mauersberger, K. *Geophys. Res. Lett.* **1988**, *15*, 1507–1510.
- (31) Thibert, E.; Domine, F. J. *Phys. Chem. B* **1997**, *101*, 3554–3565.
- (32) Thibert, E.; Domine, F. J. *Phys. Chem. B* **1998**, *102*, 4432–4439.
- (33) Brandani, V.; Di Giacomo, G.; Foscolo, P. U. *Ind. Eng. Chem. Process Des. Dev.* **1980**, *19*, 179–185.
- (34) Domine, F.; Thibert, E.; Silvente, E.; Legrand, M.; Jaffrezou, J. L. *J. Atmos. Chem.* **1995**, *21*, 165.
- (35) Capolo, L. Contribution à l'étude des hétérogénéités de déformation viscoplastique de la glace Ih mono et multi cristalline: essais de compres-

sion in-situ sous rayonnement X. Ph.D. Thesis, Université Joseph Fourier, Grenoble, France, 2007.

(36) Spitler, D.; Lantrip, J.; Nee, J. G.; Smith, D. A. *Fundamentals of tool design*; Society of Manufacturing Engineers: Dearborn, MI, 2003.

(37) Houdier, S.; Perrier, S.; Defrancq, E.; Legrand, M. *Anal. Chim. Acta* **2000**, *412*, 221–233.

(38) Philibert, J. *Diffusion et transport de matière dans les solides*; Les ed.s de Physique: Les Ulis, France, 1990.

(39) Lamb, D.; Hobbs, P. V. *J. Atmos. Sci.* **1971**, *28*, 1506–1509.

(40) Beckmann, W.; Lacmann, R. *J. Cryst. Growth* **1982**, *58*, 433–442.

(41) Hutterli, M. A.; McConnell, J. R.; Chen, G.; Bales, R. C.; Davis, D. D.; Lenschow, D. H. *Atmos. Environ.* **2004**, *38*, 5439–5450.

(42) Jacobi, H.; Frey, M. M.; Hutterli, M. A.; Bales, R. C.; Schrems, O.; Cullen, N. J.; Steffen, K.; Koehler, C. *Atmos. Environ.* **2002**, *36*, 2619–2628.

(43) Weller, R.; Schrems, O.; Boddenberg, A.; Gäb, S.; Gautrois, M. *J. Geophys. Res.* **2000**, *105*, 14401–14412.

(44) Grosjean, D.; Grosjean, E.; Moreira, L. F. R. *Environ. Sci. Technol.* **2002**, *36*, 1389–1395.

(45) Odabasi, M.; Seyfioglu, R. *Atmos. Environ.* **2005**, *39*, 5149–5156.

(46) Lu, H.; Cai, Q.; Wen, S.; Chi, Y.; Guo, S.; Sheng, G.; Fu, J.; Antizar-Ladislao, B. *Atmos. Res.* **2009**, *94*, 363–372.

(47) Correa, S. M.; Arbilla, G.; Martins, E. M.; Quitério, S. L.; de Souza Guimarães, C.; Gatti, L. V. *Atmos. Environ.* **2010**, *44*, 2302–2308.

(48) Crank, J.; Nicolson, P. *Adv. Comput. Math.* **1996**, *6*, 207–226.

(49) Domine, F.; Xueref, I. *Anal. Chem.* **2001**, *73*, 4348–4353.

(50) Domine, F.; Cabanes, A.; Legagneux, L. *Atmos. Environ.* **2002**, *36*, 2753–2765.

(51) Collignon, B.; Picaud, S. *Chem. Phys. Lett.* **2004**, *393*, 457.

(52) Winkler, A. K.; Holmes, N. S.; Crowley, J. N. *Phys. Chem. Chem. Phys.* **2002**, *4*, 5270.

JP108907U